

Article

A Computational Simulation Study of Fluid Mechanics of Low-Speed Wind Tunnel Contractions

Yi-Huan Kao ^{1,*}, Zhou-Wei Jiang ² and Sheng-Cyuan Fang ¹

¹ Center for Measurement Standard, Industrial Technology Research Institute, No. 195, Sec. 4, Chung Hsing Rd., Chutung, Hsinchu 31040, Taiwan; georgefan@itri.org.tw

² Intelligent Machinery Technology Center, Industrial Technology Research Institute, No. 195, Sec. 4, Chung Hsing Rd., Chutung, Hsinchu 31040, Taiwan; JiangZW@itri.org.tw

* Correspondence: yihuankao@gmail.com; Tel.: +886-922-933-234

Academic Editor: Meir Teitel

Received: 6 March 2017; Accepted: 2 May 2017; Published: 11 May 2017

Abstract: In this work, the fluid mechanics performance of four different contraction wall shapes has been studied and compared side-by-side by computational simulation, and the effect of contraction cross-sectional shape on the flow uniformity at the contraction exit has been included as well. A different contraction wall shape could result in up to an extra 4% pressure drop of a closed-loop wind tunnel, and the contraction wall shape has a stronger influence on the pressure loss than the contraction cross-sectional shape. The first and the second derivatives from different wall shape equations could provide a hint for qualitatively comparing the flow uniformity at the contraction exits. A wind tunnel contraction with an octagonal shape provides not only better fluid mechanics performance than that with a circular or a square cross-sectional shape, but also lower manufacturing costs. Moreover, a smaller blockage ratio within the test section can be achieved by employing an octagonal cross-sectional shape instead of a circular cross-sectional shape under the same hydraulic diameter circumstance. A wind tunnel contraction with an octagonal cross-sectional shape is recommended to be a design candidate.

Keywords: wind tunnel contraction; contraction wall shape; contraction cross-sectional shape; computational fluid dynamics

1. Introduction

In the fields of fluid mechanics research, full/scaled model testing, and airspeed calibration, wind tunnel has a critical role. For airspeed calibration, both ISO17713-1 [1] and ASTM D5096-02 [2] documents recommend that a wind tunnel facility should be used to calibrate or to test the performance of a rotating anemometer. Additionally, both ISO 17713-1 and ASTM D5096-02 request that the flow uniformity and the turbulence intensity should be smaller than 1% difference in transversal velocity profile and less than 1% within the test section of a wind tunnel, respectively. These two requirements are intended to minimize the calibration or the measurement error due to the non-uniform flow profile and the flow fluctuation. In the field of airspeed calibration or metrology, the testing environments are commonly provided by wind tunnels, thus the homogeneity among wind tunnels makes people confident that the world activities are sharing a common perception of quantity measurement. In several national metrology institutes, such as the National Institute of Standards and Technology (NIST), National Metrology Institute of Japan (NMIJ), Korea Research Institute of Standards and Science (KRISS), and National Measurement Laboratory (NML), wind tunnels are adopted to establish their airspeed measurement standards [3,4]. The validation of flow condition via experiment or simulation is also quite essential for a new wind tunnel [5–7].

The contraction is the most critical component of a wind tunnel to influence the flow quality within the test section since it is located just upstream of the test section. The air flow is accelerated through a contraction to the test section with reduced flow turbulence and flow velocity variation within the test section. In general, the contraction ratio, the contraction length, and the contraction wall curve are the three dominant design factors of a wind tunnel, and many studies about these three parameters have been done to provide the design guidance for a contraction. Batchelor [8] has derived the factors of reduction of mean velocity variation and turbulence intensity for axisymmetric contractions by using the rapid distortion theory to state that a contraction is more effective in suppressing velocity variation and turbulence intensity in the longitudinal direction than those in the lateral direction. The contraction ratio is the most critical factor in determining the mean flow uniformity at the contraction exit, which has been stated by Hussain and Ramjee [9]. Metha and Bradshaw [10] have suggested that a contraction ratio between 6 and 9 are normally sufficient for smaller wind tunnels to generate an acceptable flow quality. Wind tunnels adopted for airspeed calibration are always designed by an even higher contraction ratio for obtaining an even better flow quality. For example, the contraction ratio of NIST's wind tunnel is up to 14.52 and 18.15 for the lower speed and the higher speed test sections, respectively [11].

Although a very long contraction can be used for avoiding flow separation, it will also result in higher material cost, larger occupied space, and thicker exit boundary layer. Actually, the contraction length depends on the contraction angle determined by designers. Hernández et al. [12] have recommended taking a contraction angle of 12° for a reasonable length and a good fluid dynamic performance. Several studies about the contraction wall shape have been conducted in the last several decades. A combination of two symmetric third-order polynomial curves with appropriate conditions, such as the coordinate and the slope of the inflection point, the entrance of the wide end, and the exit of the narrow end, has been recommended by Hernández [12]. Su [13] has proposed matching a third-order polynomial curve at the contraction entrance and a higher-order polynomial curve at the contraction exit. Bell and Mehta [14] have conducted a numerical analysis to conclude that a fifth-order polynomial curve can perform optimally in terms of avoiding flow separation, giving minimum boundary layer thickness, and providing better flow uniformity, as compared to a third-order polynomial, a seventh-order polynomial, and a combination of two symmetric matched cubic curves. The fifth-order polynomial curve proposed by Bell and Mehta [14] might be one of the most popular contraction wall shape equations because it has been proved to deliver good aerodynamic performances in many wind tunnels. A combination of two third-order polynomial curves has been derived by Fang et al. [15] for the contraction having a square cross-sectional shape. A good agreement between the numerical results and the experimental results has been shown at a contraction exit velocity of 15 m/s. Bouriga et al. [16] have suggested that the details of the flow structure of a wind tunnel depend on the actual contraction geometry. Therefore, the present work aims to establish a benchmark for investigating the fluid mechanics performance in terms of pressure drop along a contraction, exit flow uniformity, and boundary layer thickness from different contraction wall shapes which have not been studied and compared side-by-side together.

Another unclear issue is the cross-sectional shape of a contraction. Ideally, an axisymmetric contraction with circular cross-sectional shape is believed to be the optimal choice for achieving a uniform flow. However, from the aspect of a manufacturing concern, a rectangular, square or octagonal design is often considered as well. The possible occurrence of secondary flows near the corners forming the intersection of the sidewalls in three-dimensional, non-circular contraction has been known for a long time [17]. Although, Metha [18] has mentioned that the corner flow for a well-designed contraction is localized and does not affect the flow quality over most of the span in the test section. The published literature discussing the cross-sectional shape effect on the fluid mechanics performance of a well-designed contraction is still very limited. Therefore, the fluid mechanics performance also will be compared for three different common cross-sectional shapes, namely, circle, square, and octagon, in the present work.

2. Problem Formulation

2.1. Contraction Dimensions

In the present work, the contraction size is based on an ongoing project for upgrading the wind tunnel for air speed standard at the National Measurement Laboratory (NML). Three different cross-sectional shapes, i.e., circle, square, and octagon are investigated. The hydraulic diameters of the entrance and the exit are 1100 mm and 350 mm, respectively, resulting in a contraction ratio of 9.88. The total length of computational domain is 2200 mm ($-200 \text{ mm} \leq x \leq 2000 \text{ mm}$), as shown in Figure 1, including a leading portion of 200 mm ($-200 \text{ mm} \leq x \leq 0 \text{ mm}$), a contraction portion of 1800 mm ($0 \text{ mm} \leq x \leq 1800 \text{ mm}$), and a trailing portion of 200 mm ($2000 \text{ mm} \leq x \leq 2200 \text{ mm}$). The equations of four contraction wall shapes are tabulated in Table 1.

Table 1. Equations for four investigated contraction (CT) wall shapes.

Contraction Case	Original Equation	Adopted Equation
CT #1 [14]	$y = \left(-6\left(\frac{x}{L}\right)^5 + 15\frac{x}{L}^4 - 10\left(\frac{x}{L}\right)^3\right) (H_i - H_o) + H_i$	$y = \left(-6\left(\frac{x}{1800}\right)^5 + 15\left(\frac{x}{1800}\right)^4 - 10\left(\frac{x}{1800}\right)^3\right) (175 - 550) + 175$
CT #2 [15]	$y = (H_o - H_i) \left[1 - \frac{1}{x_m^2} \left(\frac{x}{L}\right)^3\right] + H_i, x < x_m$ $y = \frac{(H_o - H_i)}{(1 - x_m)^2} \left(1 - \frac{x}{L}\right)^3 + H_i, x \geq x_m$	$y = (175 - 550) \left[1 - 4\left(\frac{x}{1800}\right)^3\right] + 550, x < 900$ $y = \frac{(175 - 550)}{(1 - 0.5)^2} \left(1 - \frac{x}{1800}\right)^3 + 550, x \geq 900$ where, $x_m = 0.5L = 900$
CT #3	$y = a + bx + cx^2 + dx^3$ $y(x = 0) = 175$ $y(x = 1800) = 550$ $\frac{dy}{dx}(x = 0) = 0$ $\frac{dy}{dx}(x = 1800) = 0$	$y = 175 + 3.4722 \times 10^{-4}x^2 - 1.2860 \times 10^{-7}x^2$
CT #4 [12]	$y = a_1 + b_1x + c_1x^2 + d_1x^3,$ $0 \leq x \leq 900$ $y = a_2 + b_2x + c_2x^2 + d_2x^3,$ $900 \leq x \leq 1800$ $y(x = 0) = 175$ $y(x = 900) = 362.5$ $y(x = 1800) = 550$ $\frac{dy}{dx}(x = 0) = 0$ $\frac{dy}{dx}(x = 900) = 0.35$ $\frac{dy}{dx}(x = 1800) = 0$	$y = 175 + 3.0556 \times 10^{-4}x^2 + 8.2305 \times 10^{-8}x^3,$ $0 \leq x \leq 900$ $y = 40 + 0.3x + 1.3889 \times 10^{-4}x^2 + 8.2305 \times 10^{-8}x^3,$ $900 \leq x \leq 1800$

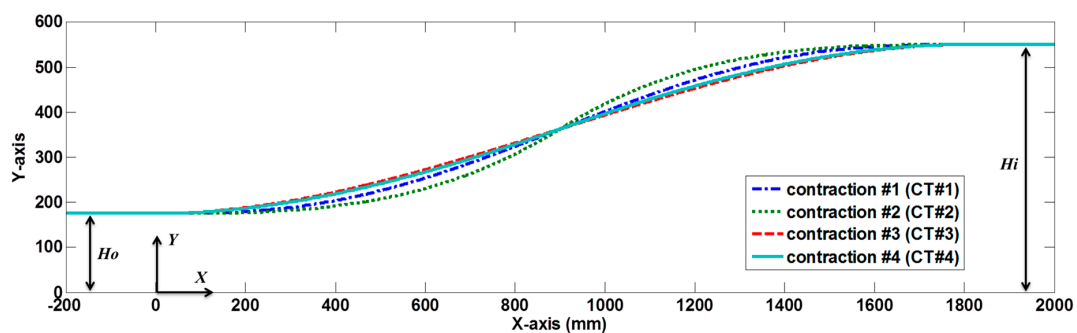


Figure 1. Four investigated contraction wall shapes.

2.2. Computational Fluid Dynamics Model

The flow field is assumed to be steady, three-dimensional, incompressible and turbulent. The working fluid is air and assumed as an ideal gas. The computational work is meshed and calculated via ANSYS FLUENT R14.5. Menter’s shear stress transportation (SST) k- ω model with double precision

option is adopted as the turbulent model. SST $k-\omega$ model is a combination of the standard $k-\epsilon$ model in the free stream region and Wilcox $k-\omega$ model in the wall regions. This model is capable of predicting the flow near the wall more accurately [19]. Also, the study from Bouriga et al. [20] has shown that SST $k-\omega$ model is proper to be used for the investigation of the flow in the contraction. The SIMPLE algorithm is utilized for pressure-velocity coupling correction and the second-order upwind scheme is applied for the equations of momentum, turbulent kinetic energy and specific dissipation rate. The residuals for continuity, momentum, and turbulent equations are aimed to be less than 1×10^{-7} .

2.3. Boundary Conditions

In the present work, two different cases with contraction exit velocities of 6 m/s and 60 m/s are studied as outlet boundary conditions, because the target operating velocity of NML's standard wind tunnel is up to 60 m/s. As the studied contraction ratio is 9.88, thus the uniform flow profiles with contraction entrance velocities of 0.608 m/s and 6.075 m/s are designated as inlet boundary conditions. According to Batchelor [8], a contraction ratio of 9.88 can reduce the axial velocity fluctuation by a factor of 0.24. Therefore, the turbulence intensity of axial velocity at the contraction exit will become around 40 times smaller than that at the contraction entrance. The turbulence intensity is defined as a ratio of the root-mean-square of the turbulent velocity fluctuations to the mean velocity. The turbulence intensities at the contraction entrance and exit for the case with contraction exit velocity of 6 m/s are designated as 40% and 1%, respectively, in order to be consistent with the turbulence intensity less than 1% suggested by both ISO and ASTM documents [1,2]. For the case with the contraction exit velocity of 60 m/s, the turbulence intensities of the contraction entrance and exit are designated as 20% and 0.5%, respectively, because turbulence intensity usually decreases with increasing the mean velocity. Furthermore, a sensitivity study has been conducted with different values of turbulent intensity at the contraction entrance and exit to show that the turbulence intensity does not have a strong influence on the simulation results. The boundary conditions for the two cases are summarized in Table 2. No-slip conditions for the velocity are imposed on the contraction walls.

Table 2. Designations of boundary conditions.

Case	Entrance	Exit
$V_{ex} = 6 \text{ m/s}$	uniform velocity profile = 0.608 m/s turbulent intensity = 40% hydraulic diameter = 1100 mm	gauge pressure = 0 turbulent intensity = 1% hydraulic diameter = 350 mm
$V_{ex} = 60 \text{ m/s}$	uniform velocity profile = 6.075 m/s turbulent intensity = 20% hydraulic diameter = 1100 mm	gauge pressure = 0 turbulent intensity = 0.5% hydraulic diameter = 350 mm

2.4. Model Validation, Mesh Setting, and Mesh Independent Test

A model validation study is conducted by duplicating the contraction geometry and comparing the experiment and numerical results provided by Ref. [15]. The mean velocity profiles at the selected cross-sections are shown in Figure 2. The results for model validation show an agreement with the results provided by Ref. [15] at $x/L = 0.5$ and carry out a more reasonable prediction, as compared to the numerical results in Ref. [15] at $x/L = 1$. The velocity profile at the contraction exit should show a core region with higher velocity surrounding by a low-velocity region due to friction effect, as displayed by the experimental results and the simulation results conducted in this work. However, the computational fluid dynamics (CFD) results from Ref. [15] fail to predict that.

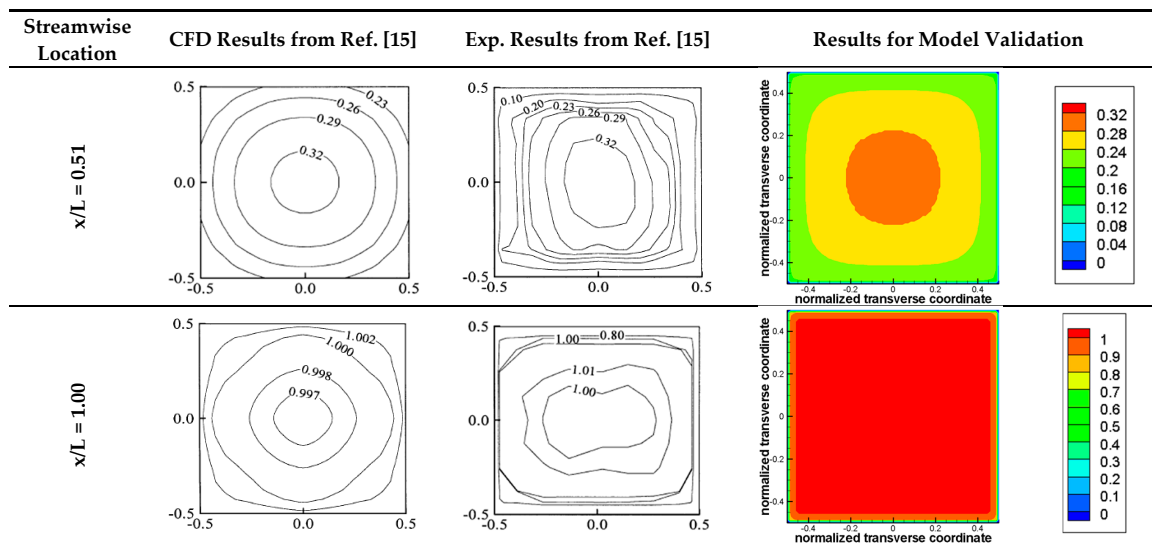


Figure 2. Comparisons with results from Fang et al. [15]. Reproduced with permission from Fang et al., J. Wind Eng. Ind. Aerodyn.; published by Elsevier, 2001.

Around 1.2×10^6 structured hexahedral cells are used for all the investigated cases in this study. An example mesh setting for the case with CT #1 is shown in Figure 3. A mesh independent test has been performed for the case with CT #1 by comparing the calculated results with about 1.2×10^6 and 2.2×10^6 cells. Figure 4 shows the calculated pressure and velocity profiles which almost overlap each other, in particular, within the highly concerned boundary layer region, from two different mesh density settings. The relative differences for pressure profile along the centerline, velocity profile along the centerline, and transversal velocity profile at contraction exit are around 0.09%, 0.02%, and 0.11%, respectively, when the case of 1.2×10^6 cells is used as the reference. From the analysis of variance (ANOVA), the p -values of pressure profile along the centerline, velocity profile along the centerline and velocity profile at contraction exit between these two mesh settings are all much less than 10^{-10} , when the significant level is assumed as 0.01. It means that the mesh setting around 1.2×10^6 cells is sufficiently dense to capture the flow physics and to evaluate the fluid mechanics performance of a contraction. For the mesh setting around 1.2×10^6 cells, the dimensionless wall distances (y^+) within the boundary layer region are around 40 and 280 for the cases with contraction exit velocity of 6 m/s and 60 m/s, respectively. It means that the wall-adjacent cell's centroid is located within the log-law layer to justify the enhanced wall treatment.

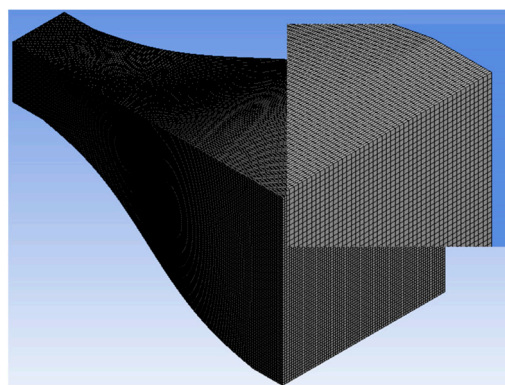


Figure 3. A view of example mesh setting.

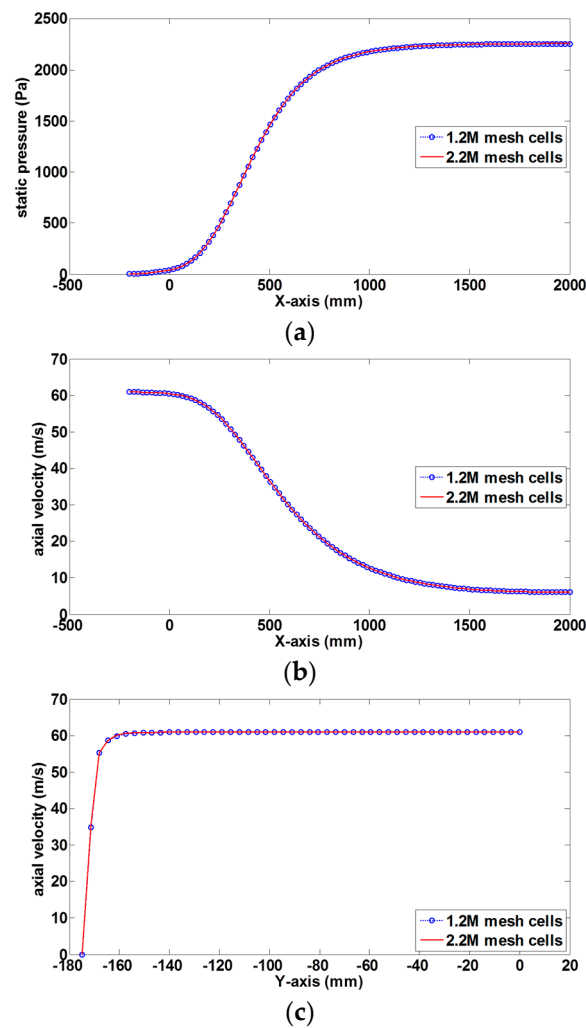


Figure 4. Pressure and velocity profiles along centerline and velocity profiles from two different mesh density settings, (a) pressure profile along centerline; (b) velocity profile along centerline; (c) velocity profile at contraction exit.

3. Results and Discussion

3.1. Effect of Contraction Wall Shape

This section will focus on the effect of contraction wall shape, considering the axisymmetric, circular cross-sectional contractions.

Figure 5 exemplifies the calculated velocity contour for the case of CT #1 at an exit velocity of 60 m/s. In fact, all four investigated contractions deliver barely distinguishable velocity contours. However, CT #2 needs a higher static upstream pressure to accelerate the flow up to 60 m/s at the contraction exit. The 80 Pa pressure loss of the CT #2 is higher than the other contractions: 72 Pa, 63 Pa, and 64 Pa for CT #1, CT #3, and CT #4, respectively, as listed in Table 3. Taking a closed-loop wind tunnel with the operating velocity of 60 m/s for example, the difference in pressure loss between CT #2 and CT #3 is around 17 Pa, which amounts to about 4% of the total pressure loss, as shown in Table 4. The pressure loss of a contraction might be a concern about the long-term operating cost and a fan selection when the operating velocity of a wind tunnel is up to 60 m/s or even up to 100 m/s.

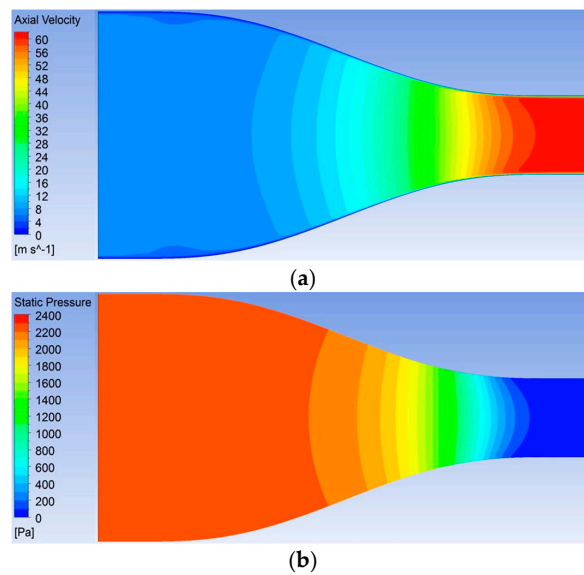


Figure 5. Calculated (a) axial velocity and (b) static pressure contours for the case with CT #1 having circle cross-sectional shape and $V_{ex} = 60$ m/s.

Table 3. Pressure drops along investigated contractions ($V_{ex} = 60$ m/s).

Case	Cross-Sectional Shape		
	Circle	Square	Octagon
CT #1	72 Pa	71 Pa	65 Pa
CT #2	80 Pa	78 Pa	70 Pa
CT #3	63 Pa	58 Pa	58 Pa
CT #4	64 Pa	65 Pa	59 Pa

Table 4. Estimated pressure drops on components of investigated closed-loop wind tunnel ($V_{ex} = 60$ m/s).

Component	Pressure Drop (Pa)	Percentage
honeycomb	12	2.9%
5 screen meshes	160	39.3%
contraction	64	15.6%
test section	79	19.3%
diffuser	37	9.0%
4 turning corners	57	13.9%
total	409	100%

The velocity profiles at the contraction exits are shown in Figure 6. The velocity profile from CT #4 shows a thinner boundary layer at the exit in the case of either $V_{ex} = 6$ m/s or $V_{ex} = 60$ m/s. The boundary layer thicknesses developed at the contraction exit by the CT #1, CT #2 and CT #3 are almost identical. The core regions, covering 90% and 88% of the central cross-section span are not influenced by the boundary layer in the case of $V_{ex} = 60$ m/s and $V_{ex} = 6$ m/s, respectively. The slight difference should be attributed to the higher velocity effect, i.e., higher Reynolds number, for suppressing the growth of boundary layer in the case of $V_{ex} = 60$ m/s. The axial velocity standard deviations within the core region of the four investigated contractions are listed in Table 5. The axial velocity standard deviation of CT #2 is higher than those of the other three contractions, while the other three contractions have very similar results. This might result from the higher first and second derivatives, i.e., the slope and the change of slope, of CT #2 than those of the other three contractions at the inflection point ($x = 900$ mm), as shown in Figure 7. It means that the contraction wall outline of CT #2 changes more rapidly than the others near the inflection point and results in a higher turbulence

kinetic energy ratio at the downstream of the inflection point ($x < 900$ mm) when the turbulence kinetic energy at the contraction inlet is used as the reference, as shown in Figure 8. The higher turbulent kinetic energy within CT #2 accounts for the higher axial velocity standard deviation at the exit. Although the non-zero second-derivative values are observed at both ends of the contraction portions of CT #3 and CT #4, the long enough parallel leading and trailing portions might be able to compensate the non-zero second derivatives at both ends. The first and the second derivatives from different contraction wall shape equations might provide a hint for qualitatively comparing the exit flow quality from the different contractions.

Table 5. Axial velocity standard deviations within core region of investigated contractions.

Case		Cross-Sectional Shape		
		Circle	Square	Octagon
$V_{ex} = 6$ m/s	CT #1	0.014 m/s	0.014 m/s	0.012 m/s
	CT #2	0.018 m/s	0.016 m/s	0.012 m/s
	CT #3	0.013 m/s	0.012 m/s	0.010 m/s
	CT #4	0.012 m/s	0.012 m/s	0.010 m/s
$V_{ex} = 60$ m/s	CT #1	0.072 m/s	0.064 m/s	0.051 m/s
	CT #2	0.097 m/s	0.073 m/s	0.052 m/s
	CT #3	0.064 m/s	0.052 m/s	0.042 m/s
	CT #4	0.059 m/s	0.054 m/s	0.045 m/s

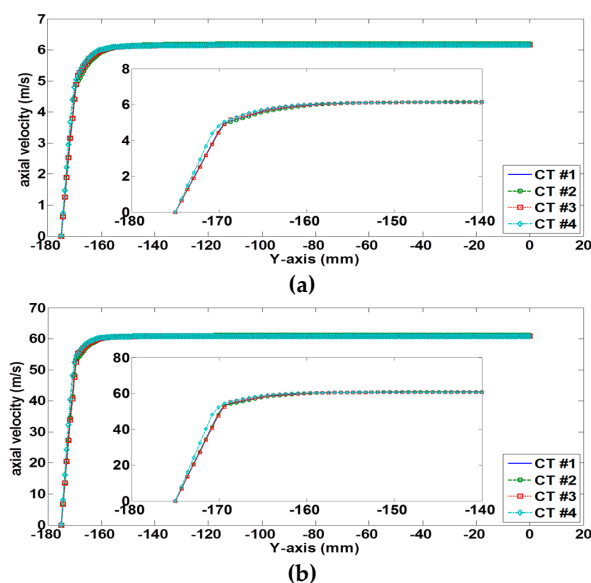


Figure 6. Axial velocity profiles at the circular cross-sectional contraction exits, (a) $V_{ex} = 6$ m/s; (b) $V_{ex} = 60$ m/s.

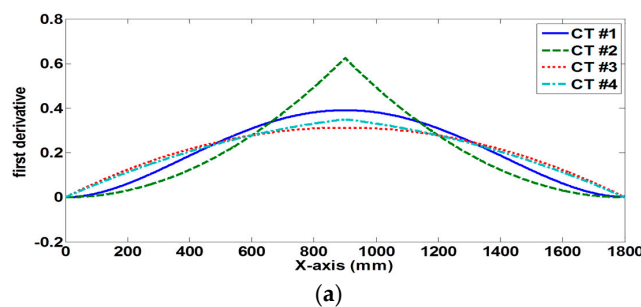


Figure 7. Cont.

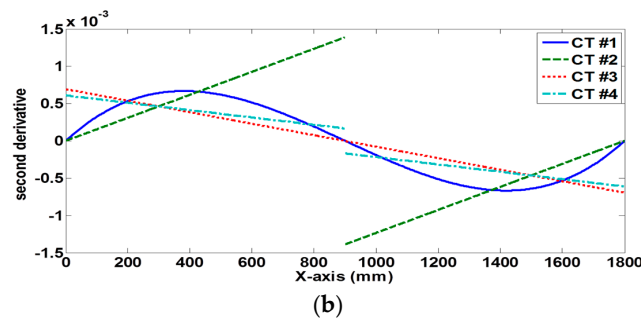


Figure 7. First (a) and second (b) derivatives of contraction wall equations.

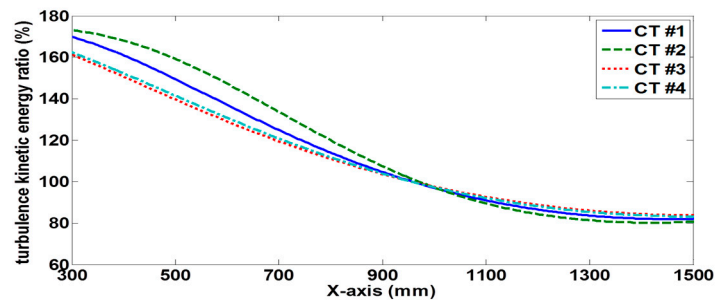


Figure 8. Turbulence kinetic energy ratio change along the wind tunnel wall.

3.2. Effect of Contraction Cross-Sectional Shape

The pressure losses along the contractions with the cross-sectional shapes of square and octagon are listed in Table 3 as well. The general observation from the square and the octagonal cross-sectional contractions is consistent with that from the circular cross-sectional contractions, with CT #2 having the highest pressure loss. The octagonal cross-sectional shape shows the overall lower pressure loss, as compared to the other cross-sectional shape among four different contraction wall shapes. For the same contraction wall shape, the differences in pressure loss among the three different cross-sectional shapes are less than 10 Pa. As afore-mentioned for the circular cross-sectional shape, the differences in pressure loss could be up to 17 Pa. It means that the wall shape is a more dominant factor for the pressure loss along a contraction than the cross-sectional shape regarding the pressure loss.

The axial velocity profiles at the contraction exits from the square and octagonal cross-sectional shapes are shown in Figures 9 and 10, respectively. All four investigated contraction wall shapes have almost identical boundary layer thickness at the contraction exit for a square cross-sectional shape. For the octagonal cross-sectional shape, CT #2 shows the slightly thicker boundary layer and the highest axial velocity standard deviations at the contraction exit (Table 5), as compared to the other three contraction wall shapes. This is consistent with the observation from the circular cross-sectional shapes.

In Figure 11, presented for CT #1 as an example, the corner flow is localized and does not result in a separation flow to significantly affect most of the test section span. The present results are consistent with the statement of Metha [17]. However, the cross-sectional shape still influences the boundary layer thickness and the axial velocity standard deviation within the core region at the contraction exit. The case with an octagonal cross-sectional shape shows a better performance in fluid mechanics in terms of the thinner boundary layer (Figure 12), the lower axial velocity standard deviation (Table 5), and the lower pressure loss (Table 3) than the other cases with a circular or a square cross-sectional shape. Moreover, our experience shows that the octagonal one also has the lower difficulty of manufacturing and cost.

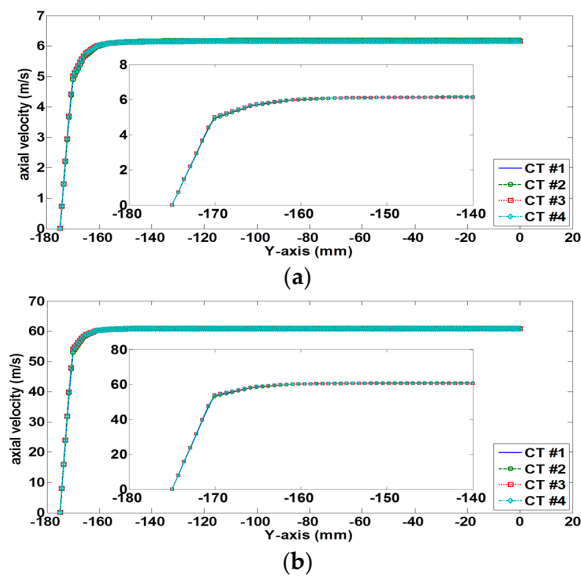


Figure 9. Axial velocity profiles at the square cross-sectional contraction exits, (a) $V_{ex} = 6 \text{ m/s}$; (b) $V_{ex} = 60 \text{ m/s}$.

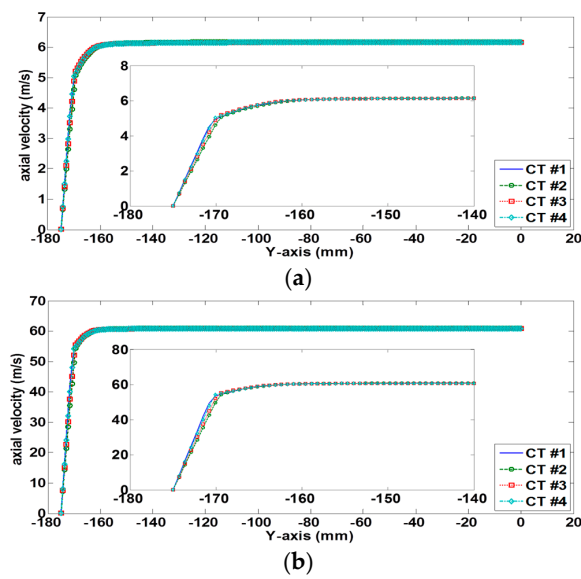


Figure 10. Axial velocity profiles at the octagonal cross-sectional contraction exits, (a) $V_{ex} = 6 \text{ m/s}$; (b) $V_{ex} = 60 \text{ m/s}$.

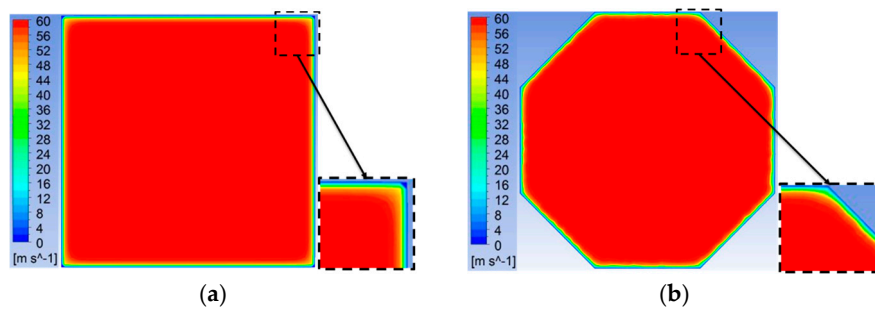


Figure 11. Axial velocity contours at contraction exits (CT #1), (a) square cross-sectional shape; (b) octagonal cross-sectional shape.

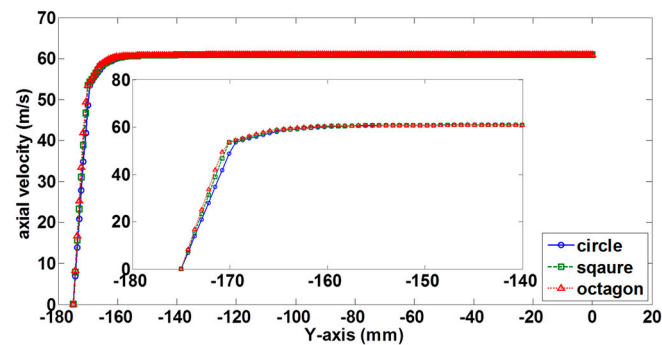


Figure 12. Axial velocity profiles at contraction exits (CT #1).

4. Conclusions

In this work, computational simulations on the fluid mechanics of wind tunnel contractions have been conducted. Four different contraction wall shapes and three common cross-sectional shapes, namely, circle, square and octagon, are studied. The main conclusions of this work are highlighted as follows:

1. Different contraction wall shapes investigated in this study result in pressure loss difference up to 17 Pa, contributing about 4% in the pressure loss of the entire wind tunnel system. The effect of cross-sectional shape would only lead to pressure loss differences less than 10 Pa. Thus, the wall shape is more critical than the cross-sectional shape of a wind tunnel.
2. The first and the second derivatives of different contraction wall shape equations could provide a hint for qualitatively comparing the flow characteristics at the contraction exits.
3. The octagonal cross-sectional shape of a wind tunnel shows a better fluid mechanics performance in terms of the thinner boundary layer, a lower axial velocity standard deviation within the core region at the contraction exit, and a lower pressure drop along the contraction.
4. From the aspect of an engineering application, a wind tunnel contraction with an octagonal cross-sectional shape has not only better flow performance than that with a circular or square cross-sectional shape but also the lower difficulty of manufacturing and cost according to our experience. Moreover, as compared to the circular cross-sectional shape, the octagonal cross-sectional shape has a larger cross-sectional area to result in a smaller blockage ratio within the test section under the same hydraulic diameter circumstance. An octagonal cross-sectional shape is recommended as a design candidate of wind tunnel contraction.

Author Contributions: Yi-Huan Kao and Zhou-Wei Jiang conceived and performed the computational simulations; Yi-Huan Kao and Sheng-Cyuan Fang analyzed the data; Yi-Huan Kao and Zhou-Wei Jiang wrote the paper.

Conflicts of Interest: The authors declare no conflict of interest.

Abbreviations

The following abbreviation is used in this manuscript:

CT	contraction
H_i	half height of contraction entrance
H_o	half height of contraction exit
L	length of contraction portion
V_{ex}	exit axial velocity
X_m	equal to x_m/L
x	x coordinate
x_m	location of inflection point
y	y coordinate

References

1. International Organization for Standardization. *Meteorology—Wind Measurements—Part 1: Wind Tunnel Test Methods for Rotating Anemometer Performance*; ISO 17713-1: 2007(E); BSI: London, UK, 2007.
2. ASTM International. *Standard Test Method for Determining the Performance of a Cup Anemometer or Propeller Anemometer*; D5096-02; ASTM: West Conshohocken, PA, USA, 2011.
3. Chun, S. *Air Speed Measurement Standards Using Wind Tunnels, Wind Tunnels and Experimental Fluid Dynamics Research*; InTech: Rijeka, Croatia, 2011; pp. 173–197.
4. Terao, Y.; Choi, Y.M.; Gutkin, M.; Jian, W.; Shinder, I.; Yang, C.-T. Final Report on the APMP Air Speed Key Comparison (APMP.M.FF-K3). *Metrologia* **2010**, *47*, 1–31. [[CrossRef](#)]
5. Moonen, P.; Blocken, B.; Roels, S.; Carmeliet, J. Numerical modeling of the flow conditions in a closed-circuit low-speed wind tunnel. *J. Wind Eng. Ind. Aerodyn.* **2006**, *94*, 699–723. [[CrossRef](#)]
6. Lastra, M.R.; Oro, J.M.F.; Vega, M.G.; Marigorta, E.B.; Morros, C.S. Novel design and experimental validation of a contraction nozzle for aerodynamic measurement in a subsonic wind tunnel. *J. Wind Eng. Ind. Aerodyn.* **2013**, *118*, 35–43. [[CrossRef](#)]
7. Calautit, J.K.; Chaudhry, H.N.; Hughes, B.R.; Sim, L.F. A validated design methodology for a closed-loop subsonic wind tunnel. *J. Wind Eng. Ind. Aerodyn.* **2014**, *125*, 180–194. [[CrossRef](#)]
8. Batchelor, G.K. *The Theory of Homogeneous Turbulence*; Cambridge University Press: Cambridge, UK, 1953; pp. 68–75.
9. Hussain, A.K.M.F.; Ramjee, V. Effects of the axisymmetric contraction shape on incompressible turbulent flow. *J. Fluids Eng.* **1976**, *98*, 58–68. [[CrossRef](#)]
10. Metha, R.D.; Bradshaw, P. Design rules for small low speed wind tunnels. *Aeronaut. J.* **1979**, *83*, 443–449.
11. Yeh, T.T.; Hall, J.M. *Airspeed Calibration Service*; National Institute of Standards and Technology (NIST): Gaithersburg, MD, USA, 2007; pp. 250–279.
12. Hernández, M.A.G.; López, A.I.M.; Jarzabek, A.A.; Perales, J.M.P.; Wu, Y.; Sun, X.X. Design Methodology for a Quick and Low-Cost Wind Tunnel. In *Wind Tunnel Designs and Their Diverse Engineering Applications*; InTech: Rijeka, Croatia, 2013; pp. 3–28.
13. Su, Y. Flow analysis and design of three-dimensional wind tunnel contractions. *AIAA J.* **1991**, *29*, 1912–1920.
14. Bell, J.H.; Mehta, R.D. *Contraction Design for Small Low-Speed Wind Tunnels*; NASA Ames Research Center: Moffett Field, CA, USA, 1988.
15. Fang, F.; Chen, J.C.; Hong, Y.T. Experimental and analytical evaluation of flow in a square-to square wind tunnel contraction. *J. Wind Eng. Ind. Aerodyn.* **2001**, *89*, 247–262. [[CrossRef](#)]
16. Bouriga, M.; Taher, R.; Morency, F.; Weiss, J. Numerical investigation of secondary flows in a constant-width wind-tunnel contraction. *Aeronaut. J.* **2015**, *119*, 613–630. [[CrossRef](#)]
17. Bradshaw, P.; Pankurst, R.C. The design of low-speed wind tunnels. *Prog. Aerosp. Sci.* **1964**, *5*, 1–69. [[CrossRef](#)]
18. Mehta, R.D. Aspects of the Design and Performance of Blower Wind Tunnel Component. Ph.D. Thesis, Department of Aeronautics, Imperial College, University of London, London, UK, 1978.
19. Mentor, F. Two-equation eddy-viscosity turbulence models for engineering applications. *AIAA J.* **1994**, *23*, 1335–1342. [[CrossRef](#)]
20. Bouriga, M.; Lemyre-Baron, J.; Morency, F.; Weiss, J. Preliminary experimental and numerical investigations of the flow in the contraction of a boundary layer wind tunnel. *Trans. Can. Soc. Mech. Eng.* **2014**, *38*, 517–532.

